



HAL
open science

Patch-Based Super-Resolution of Arterial Spin Labeling Magnetic Resonance Images

Cédric Meurée, Pierre Maurel, Jean-Christophe Ferré, Christian Barillot

► **To cite this version:**

Cédric Meurée, Pierre Maurel, Jean-Christophe Ferré, Christian Barillot. Patch-Based Super-Resolution of Arterial Spin Labeling Magnetic Resonance Images. *NeuroImage*, 2019, 10.1016/j.neuroimage.2019.01.004 . inserm-01880726v1

HAL Id: inserm-01880726

<https://inserm.hal.science/inserm-01880726v1>

Submitted on 25 Sep 2018 (v1), last revised 25 Feb 2019 (v2)

HAL is a multi-disciplinary open access archive for the deposit and dissemination of scientific research documents, whether they are published or not. The documents may come from teaching and research institutions in France or abroad, or from public or private research centers.

L'archive ouverte pluridisciplinaire **HAL**, est destinée au dépôt et à la diffusion de documents scientifiques de niveau recherche, publiés ou non, émanant des établissements d'enseignement et de recherche français ou étrangers, des laboratoires publics ou privés.

Patch-Based Super-Resolution of Arterial Spin Labeling Magnetic Resonance Images

Cédric Meurée^{1,2}, Pierre Maurel², Jean-Christophe Ferré^{2,3}, Christian Barillot²

¹ *Siemens Healthcare SAS, Saint-Denis, France*

² *Univ Rennes, CNRS, Inria, Inserm, IRISA UMR 6074, VISAGES - ERL U 1228, F-35000 Rennes, France*

³ *CHU Rennes, Department of Neuroradiology, F-35033 Rennes, France*

Abstract

Arterial spin labeling is a magnetic resonance perfusion imaging technique that, while providing results comparable to methods currently considered as more standard concerning the quantification of the cerebral blood flow, is subject to limitations related to its low signal-to-noise ratio and low resolution. In this work, we investigate the relevance of using a non-local patch-based super-resolution method driven by a high resolution structural image to increase the level of details in arterial spin labeling images. This method is evaluated by comparison with other image dimension increasing techniques on a simulated dataset, on images of healthy subjects and on images of subjects diagnosed with brain tumors, who had a dynamic susceptibility contrast acquisition. The influence of an increase of ASL images resolution on partial volume effects is also investigated in this work.

Keywords: MRI, Arterial Spin Labeling, Super-Resolution, Denoising, Partial Volume Effects

1. Introduction

2 Cerebral perfusion corresponds to the delivery of nutrients and oxygen to
3 brain tissues. Its assessment is important for clinicians, as it has been shown
4 that abnormal perfusion patterns are often the causes or consequences of
5 pathologies [1].

6 Arterial spin labeling (ASL) is a non-invasive magnetic resonance (MR) imag-
7 ing technique that quantitatively evaluates this perfusion. Radio frequency

8 inversion pulses are applied to the blood water protons flowing through the
9 neck of the imaged subject. After a certain amount of time left for these
10 labeled protons to reach the brain, called the post-labeling delay (PLD), an
11 image is acquired, which is called the labeled image. The difference between
12 this image and a control image, acquired without the labeling step, is propor-
13 tional to brain perfusion. The cerebral blood flow (CBF) can be quantified
14 from this perfusion image [4, 5]. Recommendations regarding ASL image ac-
15 quisitions have been formulated by a consortium in the ASL "white paper"
16 [6].

17 While very promising in some aspects, ASL is, however, still subject to a
18 number of limitations. Indeed, fast acquisition techniques such as echo plan-
19 nar imaging (EPI) are required to image the dynamic process of the labeled
20 protons circulation, which generate low resolution and low signal-to-noise
21 ratio (SNR) images. For that reason, multiple label and control pairs are
22 usually acquired and averaged. However, this makes ASL subject to new
23 potential corruptions, such as movement artifacts and the introduction of
24 outlier intensity values. Moreover, small subject motion and the low resolu-
25 tion of the images involve the introduction of partial volume effects (PVE),
26 meaning that perfusion of different tissues contribute to the perfusion signal
27 observed in a single image voxel.

28 Several post-processing algorithms have been proposed to deal with these
29 limitations. Particularly, denoising methods are successfully applied to deal
30 with artifacts and outliers in ASL images [7, 8, 9, 10]. PVE correction al-
31 gorithms have also been proposed and investigated in [11, 12, 13]. These
32 methods have in common to be applied at the resolution of the acquired
33 images. While attenuating the effect of the previously listed corruptions,
34 they do not allow to increase the level of details in images. However, this
35 aspect could be of great interest, the thickness of grey matter (GM) being
36 often inferior to the size of the ASL images voxel size. In clinical conditions,
37 acquiring ASL images at higher resolutions is a challenging task, since this
38 would imply a decrease in SNR, or increase the acquisition time.

39 Various methods have been proposed in order to increase the resolution of
40 MR images facing similar low resolution properties, such as T2-weighted and
41 diffusion images, as a post-processing step. Interpolation methods can be
42 applied to MR images (trilinear interpolation, B-splines), unfortunately re-
43 sulting in blurred images. To overcome this aspect, super-resolution (SR)
44 approaches allow to reconstruct high frequency information from low reso-
45 lution data. Some of these methods are based on multiple low resolution

46 acquisitions, therefore requiring specific acquisition protocols, which can be
 47 time consuming [14]. Recently, [15, 16, 17] have adapted and extended non-
 48 local patch-based SR approaches that are independent of the acquisition
 49 process to the MRI domain. The main idea consists in using self similarities
 50 in the images to perform reconstructions at higher resolutions [18]. These
 51 methods can be applied to data commonly acquired in clinical conditions,
 52 such as T2-weighted or diffusion weighted images, thus preventing any in-
 53 crease in the acquisition time. A first application of this kind of method
 54 to pseudo-continuous ASL (pCASL) images has been proposed in [19]. The
 55 main limitation of these methods is that they require clean low resolution
 56 data as inputs, which means that denoising algorithms must first carefully
 57 be applied to the images prior to SR reconstruction.

58 In this paper, we propose a novel method to increase the resolution of ASL
 59 images, which deals with the presence of noise. This non-local patch-based
 60 SR reconstruction approach is based on the assumption of appearing simi-
 61 larities between neighborhoods in the image that is reconstructed and a high
 62 resolution (HR) structural image, generally acquired in imaging protocols.
 63 This aspect allows to increase the resolution of ASL images without extend-
 64 ing the acquisition time. The proposed method is evaluated on a simulated
 65 dataset and images of healthy subjects in order to investigate its capacity to
 66 reconstruct images close to HR ASL references. As DSC is commonly con-
 67 sidered as a reference perfusion imaging technique, we investigate the ability
 68 of our method to generate images closer to the DSC quantitative maps on
 69 images acquired on subjects diagnosed with brain tumors. In addition, we
 70 investigate the influence of a recovery of HR details on PVE.

71 The material and methods are presented in section 2, results regarding com-
 72 parisons between generated images and reference HR ASL or DSC maps in
 73 section 3, an evaluation of the influence of the SR reconstruction on PVE in
 74 section 4 and a discussion of these aspects in section 5.

75 2. Materials and Methods

76 2.1. Summary of existing similarity-based SR methods

77 The objective of super-resolution methods is to recover an unknown high
 78 resolution (HR) image x from a low resolution acquired one y . The following
 79 model explicit the relation between both images :

$$y = Mx + \eta, \tag{1}$$

80 with M a matrix representing subsampling, blurring and geometric transfor-
 81 mations, and η representing some additive noise [18, 15, 16, 17]. An optimiza-
 82 tion problem of the following form would correspond to a common approach
 83 to recover the unknown image x :

$$\tilde{X} = \arg \min_x \{ \|y - Mx\|_2^2 + \gamma\Phi(x) \}, \quad (2)$$

84 where Φ is a regularization term necessary to solve this ill-posed mini-
 85 mization problem and γ a positive parameter.

86 As shown in [16] and [17], an iterative reconstruction-correction procedure
 87 can be adopted in order to reconstruct x , which allows to avoid problems
 88 such as local minima or parameters initialization linked to this ill-posed op-
 89 timization problem. This procedure consists in two steps, corresponding to
 90 a reconstruction and a subsampling consistency constraint.

91 The reconstruction is based on the assumption that locations in a HR ac-
 92 quired structural image and the SR reconstructed one should share anatomi-
 93 cal properties, and that the structural image could therefore be used to drive
 94 the reconstruction process. This assumption leads to the choice of non-local
 95 regularization approaches, such as in [16] and [17].

96 The subsampling consistency imposes the constraint of a strict equality be-
 97 tween the downsampled version of the SR reconstructed image and the orig-
 98 inal low resolution image y , which is made possible by formulating strong
 99 assumptions about the M matrix composition. However, this constraint im-
 100 plies the need for well denoised low resolution images for the method to be
 101 consistent. Therefore, Coupé et al. [17] proposed to apply a Rician-adapted
 102 denoising filter on diffusion images before solving the optimization problem.
 103 In the case of low signal-to-noise ratio ASL images, different noise patterns
 104 can be introduced regarding the scanners, sequences or settings chosen to
 105 perform the acquisition. The use of parameters that could not be the most
 106 appropriate ones in the filtering step, could have important consequences
 107 regarding the quality of the final reconstructed image. This is the reason
 108 why we introduce a reconstruction driven by a HR structural image, while
 109 denoising the SR reconstructed image at the same time.

110 *2.2. A new SR method for ASL images*

111 The main objective of this work is to assess the relevance of using a HR
 112 anatomical image to increase the resolution of ASL images. This assumption
 113 of shared anatomical properties between structural and ASL images comes

114 from the fact that gray matter and white matter are the two tissues that
 115 contribute to the brain ASL signal, with their own perfusion characteristics
 116 (e.g. CBF and arterial arrival time) [11, 12, 13]. Following a similar idea
 117 than [15], [16] and [17], we propose a non-local patch-based method, while
 118 introducing a novel denoising strategy.

119 Because of the use of non-local patch-based approaches, both in the denois-
 120 ing and SR methods previously described [17], we propose to combine them
 121 in a unique SR image reconstruction process. A third order B-splines in-
 122 terpolation is first applied to the low resolution image in order to increase
 123 its dimension to the desired one. This initialization is followed by iterations
 124 between a non-local patch-based regularization and a fidelity term assuring
 125 the global intensities mean consistency between the initial low resolution im-
 126 age and the reconstructed one. This fidelity term differs from the one in use
 127 in the works presented in the previous section [16,17], in the sense that it
 128 involves a global image mean consistency, and not a subsampling consistency
 129 at the voxel level, therefore allowing a denoising of the reconstructed image.
 130 In the regularization term, correspondences between voxels' neighborhoods
 131 are assessed both in the reconstructed image and the structural one:

$$X_i^{t+1} = \frac{1}{Z_i} \sum_{j \in V_i} X_j^t \exp - \left(\frac{\|N(X_{i,S}) - N(X_{j,S})\|_2^2}{\beta_S \sigma_{i,S}^2} + \frac{\|N(X_i^t) - N(X_j^t)\|_2^2}{\beta \sigma_i^2} \right), \quad (3)$$

132 where X_i^t is the intensity of voxel i in the image X^t corresponding to iteration
 133 t , X_S the structural image, $N(X_i)$ and $N(X_{i,S})$ patches selected around voxel
 134 i in the ASL and structural images respectively, σ_i^2 and $\sigma_{i,S}^2$ the empirical local
 135 variances, V_i the correspondence search volume around voxel i , Z_i a scaling
 136 parameter controlling that the sum of the weights is equal to 1, and β and
 137 β_S two scalars adjusting the importance of the terms related to the ASL
 138 and structural images. The exponential weights, including an evaluation
 139 of the simultaneous similarity of voxel neighborhoods in the structural HR
 140 and reconstructed images, enable an increase in the level of details in the
 141 ASL image, while preserving features that are only visible in this image.
 142 Indeed, if neighborhoods are similar on two voxel locations in both images,
 143 the contribution in the regularization will be important. In the contrary, if
 144 a feature is only visible in one of the images, the weight will have a lower
 145 value, and have a reduced contribution in this process.
 146 The global low resolution mean value consistency corresponds to an additive

147 offset equal to the difference between the mean image value of X^t and the
 148 mean of the low resolution image Y , respectively $\mu(X)$ and $\mu(Y)$:

$$X^{t'} = X^t + (\mu(Y) - \mu(X^t)). \quad (4)$$

149 Iterations between these two steps are performed until no significant differ-
 150 ence between consecutive reconstructed images can be observed, which can
 151 be written as follows:

$$\frac{|X^{t-1} - X^{t-2}|}{|X^t - X^{t-1}|} < \tau. \quad (5)$$

152 As in [17], a coarse to fine approach is proposed where the weights β and β_S
 153 are decreased at each iteration of the process, leading to $[\beta, \beta/2, \beta/4, \dots]$ and
 154 $[\beta_S, \beta_S/2, \beta_S/4, \dots]$ respectively.

155 2.3. Validation framework

156 2.3.1. Simulated dataset

157 In order to evaluate the proposed method in a controlled environment,
 158 we constructed a simulated set of 9 CBF maps. This dataset was built
 159 from structural (MP2RAGE UNI, [20]) images acquired at a resolution of
 160 $1 \times 1 \times 1 \text{ mm}^3$ with a 3T Siemens Verio scanner and a 32-channel head-coil.
 161 Fixed CBF values were considered for gray matter (GM) and white matter
 162 (WM), equal to 70 and 25 ml/100g/min respectively [21]. These values were
 163 affected to the probability maps obtained by means of the SPM12 segmen-
 164 tation algorithm [22], leading to the application of the following equation:

$$\text{cbf}_i = p_{GM,i} \cdot 70 + p_{WM,i} \cdot 25, \quad (6)$$

165 with cbf_i the simulated CBF value at voxel i , and $p_{GM,i}$ and $p_{WM,i}$ the respec-
 166 tive PV probability values for GM and WM provided by the segmentation
 167 at the same voxel location.

168 These HR simulated CBF maps were then downsampled to a resolution of
 169 $2 \times 2 \times 2 \text{ mm}^3$ by applying a gaussian blurring before downscaling by a factor
 170 of 2 in the 3 directions. The downsampled images were then reconstructed
 171 at the original resolution using different methods: nearest neighbor inter-
 172 polation, trilinear interpolation, 3rd order B-splines interpolation and the
 173 proposed SR reconstruction method.

174 The root mean square errors (RMSE) between the original HR simulated

175 CBF maps and the reconstructed images were calculated in order to evalu-
 176 ate the ability of each method to provide reconstructed images close to this
 177 reference. As ASL images acquired in clinical conditions are usually affected
 178 by noise, commonly considered as gaussian in CBF maps due to the aver-
 179 aging of multiple label-control pairs, we also studied the behavior of each of
 180 these methods as a function of the amount of noise. Downsampled images
 181 affected by gaussian noise with standard errors corresponding to 3 to 14% of
 182 the GM CBF value were reconstructed at the original resolution in order to
 183 evaluate this behavior. Figure 1 illustrates these images generation and the
 184 processing steps.

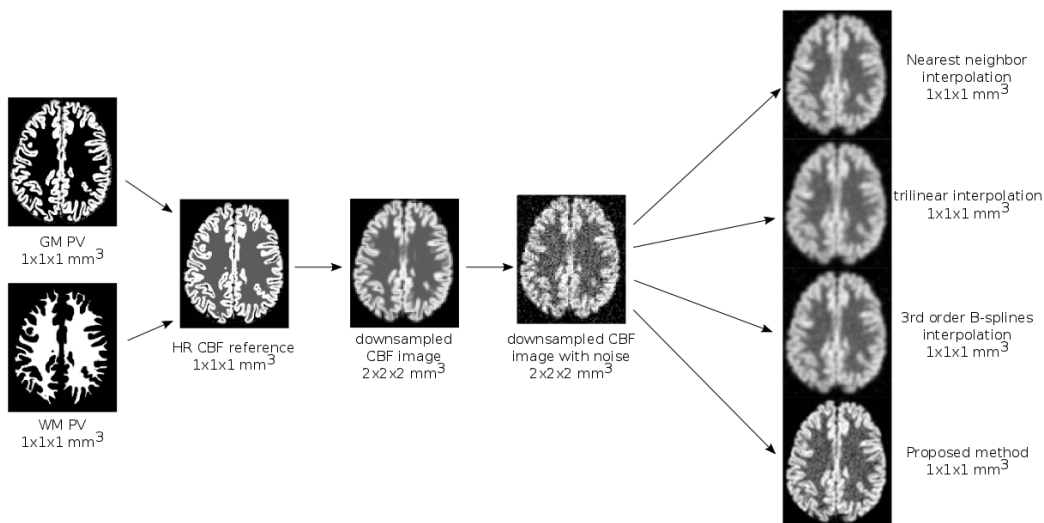


Figure 1: Pipeline describing the generation of the simulated dataset and the different reconstruction methods to be compared, applied to the downscaled and noise corrupted images.

185 2.3.2. Healthy controls

186 The SR reconstruction method was also evaluated on images acquired
 187 on 4 healthy subjects (3 females, 1 male, age = 34 ± 6 years). For each of
 188 these volunteers, images were acquired on a 3T Siemens Verio scanner with
 189 a 32-channel head-coil. The structural image consisted in a MP2RAGE UNI
 190 (resolution: $1 \times 1 \times 1 \text{ mm}^3$). pCASL (resolution: $3.5 \times 3.5 \times 5 \text{ mm}^3$, interslice
 191 gap: 1 mm, 30 control-label pairs repetitions, PLD: 1800 ms, labeling dura-
 192 tion (LD): 1800 ms, 20 slices [23]) and M0 (resolution: $3.5 \times 3.5 \times 5 \text{ mm}^3$, inter-

193 slice gap: 1 mm, 5 repetitions, 20 slices) images were acquired as the low reso-
 194 lution data used to generate the CBF maps to be reconstructed by increasing
 195 their dimensions by a factor of 2 in each direction. HR pCASL images were
 196 also acquired for the evaluation purpose (resolution: $1.75 \times 1.75 \times 2.5 \text{ mm}^3$,
 197 interslice gap: 0.5 mm, 100 control-label pairs repetitions, PLD: 1800 ms,
 198 LD: 1800 ms, 20 slices), as well as HR M0 (resolution: $1.75 \times 1.75 \times 2.5 \text{ mm}^3$,
 199 interslice gap: 0.5 mm, 10 repetitions, 20 slices). Image SNR being propor-
 200 tional to voxel volume, 100 repetitions were acquired in order to generate the
 201 HR pCASL images. While not entirely compensating for the SNR decrease
 202 in comparison with the 30 repetitions low resolution acquisitions, this repe-
 203 tition number was chosen as a compromise between scan time (10 minutes),
 204 risk of subjects motion and SNR.
 205 CBF maps were obtained by applying the general kinetic model for pCASL
 206 acquisitions [4]:

$$CBF = \frac{6000 \cdot \lambda \cdot \Delta M \cdot \exp(\frac{PLD}{T_{1,blood}})}{2 \cdot \alpha \cdot T_{1,blood} \cdot M0 \cdot (1 - \exp(-\frac{LD}{T_{1,blood}}))}, \quad (7)$$

207 with λ the blood/brain partition coefficient ($\lambda : 0.9$), α the labeling efficiency
 208 ($\alpha : 0.85$), ΔM the control-label difference, and $T_{1,blood}$ the blood T_1 relax-
 209 ation time ($T_{1,blood} : 1650 \text{ ms}$).

210 As in the case of the simulated data, RMSE values between the reconstructed
 211 images generated by the different methods and the HR pCASL CBF map,
 212 considered as the reference, were calculated.

213 2.3.3. Correlation with DSC

214 As mentioned in the introduction, Dynamic Susceptibility Contrast (DSC)
 215 imaging is often considered as a standard perfusion MR imaging technique.
 216 A contrast agent, usually gadolinium-based, is injected to the subject and
 217 the induced susceptibility effects are imaged via T2*-weighted acquisitions.
 218 In clinical conditions, this technique enables acquisitions at a higher reso-
 219 lution than ASL scans. Therefore, we studied the correlation between low
 220 resolution CBF maps obtained from pulsed ASL (PASL) images, the same
 221 images after an increase of the dimensions by a factor of 2 in each direction
 222 with different interpolation methods and the HR DSC CBF images.

223 The dataset contains images of 10 patients diagnosed with brain tumors
 224 (3 females, 7 males, age = 63 ± 13 years). Images were acquired on a 3T
 225 Siemens Verio scanner with a 32-channel head-coil. A 3D T1w sequence (res-

226 olution: $1 \times 1 \times 1 \text{ mm}^3$) was acquired, as well as a PICORE Q2TIPS PASL
 227 sequence with crushers (EPI readout, TR: 3000 ms, TE: 18 ms, FOV: $192 \times$
 228 192 mm^2 , flip angle: 90° , in plane resolution: $3 \times 3 \text{ mm}^2$, slice thick-
 229 ness: 7 mm, interslice gap: 0.7 mm, inversion time (TI): 1700 ms, bolus width
 230 (TI_1): 700 ms, 30 control-label repetitions) and a DSC sequence (GRE EPI
 231 readout, TR: 1500 ms, TE: 300 ms, FOV: $230 \times 230 \text{ mm}^2$, flip angle: 90° , in
 232 plane resolution: $1.8 \times 1.8 \text{ mm}^2$, slice thickness: 4 mm, interslice gap: 1.2 mm).
 233 The CBF maps were generated from the DSC images by use of the method
 234 proposed by Østergaard et al. [24]. The general kinetic model for PASL
 235 acquisitions was applied to the ASL scans [4]:

$$CBF = \frac{6000 \cdot \lambda \cdot \Delta M \cdot \exp\left(\frac{TI}{T_{1,blood}}\right)}{2 \cdot \alpha \cdot TI_1 \cdot M_0}, \quad (8)$$

236 The other parameters are the same as in (7), except $\alpha : 0.98$. Assuming that
 237 ASL and DSC CBF estimations are linearly correlated, as stated in Warmuth
 238 et al. [25], the Pearson correlation coefficients were calculated between the
 239 low resolution ASL CBF and the registered HR DSC CBF maps, and the SR
 240 reconstructed ASL CBF and DSC CBF maps.

241 *2.4. Implementation details*

242 An in-house image processing pipeline based on Python, Cython, Nipype [26]
 243 and SPM12 functions was used to conduct the experiments. Considering re-
 244 sults presented in [17] and our own experiments, the patch size was chosen
 245 equal to $3 \times 3 \times 3$ voxels in the non-local patched-based regularization, and
 246 the search volume to $7 \times 7 \times 7$ voxels. In order to obtain an equivalent contri-
 247 bution of the ASL and structural related terms in the reconstruction process,
 248 β and β_S were chosen to be equal. Tests and quantitative evaluations with
 249 different values on the simulated dataset and the healthy subjects images
 250 conducted to the selection of $\beta = \beta_S = 0.5$. Therefore, all results presented
 251 in the following sections have been obtained by use of these parameters.

252 **3. Results**

253 *3.1. Simulated dataset*

254 Images corresponding to reconstructions of a low resolution CBF map
 255 corrupted by gaussian noise with a standard deviation equal to 9% of the
 256 GM CBF value, which we qualitatively suppose being a close example to

257 effective low resolution acquired images, are displayed in Figure 2. The im-
 258 ages generated by use of interpolation techniques (nearest neighbor, trilinear
 259 and 3rd order B-spline interpolations) appear flattened, compared to the SR
 260 reconstructed map, which enables to recover sharp structures and edges. Ta-
 261 ble 1 confirms these observations, with lower mean RMSE values (in bold)
 262 calculated between the simulated reference images and the SR reconstructed
 263 ones than between the references and the interpolated images. In addition,
 264 the evolution of these RMSE values indicates that the more the standard
 265 deviation of noise increases, the closer to the reference the reconstructed im-
 266 age is in comparison with the interpolated images. This result is associated
 267 with the capability of the proposed method to denoise the images. Table 2
 268 provides information about the p-values obtained by applying paired t-tests
 269 between the RMSE values obtained from the proposed reconstructions and
 270 the other interpolation methods. Significant differences between the pro-
 271 posed reconstruction method and the interpolation techniques are found for
 272 levels of noise superior to 6% of the GM CBF value.

Noise std	3	6	9	11	14
Nearest neighbor	14.82 ± 0.82	15.3 ± 0.78	16.31 ± 0.80	17.72 ± 0.97	19.98 ± 1.43
Trilinear	14.80 ± 0.91	14.93 ± 0.90	15.22 ± 0.89	15.66 ± 0.86	16.38 ± 0.94
B-splines	14.01 ± 0.89	14.35 ± 0.86	15.08 ± 0.83	16.12 ± 0.85	17.78 ± 1.19
Proposed method	13.92 ± 1.05	14.05 ± 1.04	14.34 ± 1.01	14.79 ± 0.99	15.56 ± 1.08

Table 1: Means and standard deviations of the 9 RMSE values calculated between the reference HR image and the images reconstructed with nearest neighbor interpolation, trilinear interpolation, 3rd order B-splines interpolation and the proposed SR reconstruction method, with increasing levels of noise. Standard deviations of noise are expressed as percentage of the GM CBF value.

273 3.2. Healthy controls

274 Figures 3, and 4 present the images obtained from one of the 4 volunteers.
 275 Sagittal slices are shown, notably to insist on the influence of the methods on
 276 the staircase effect related to the particularly low initial resolution in the slice
 277 acquisition direction (5mm + 1mm gap). This effect is strongly corrected by
 278 the proposed SR reconstruction method. The RMSE values are reported in
 279 table 3, the proposed method providing images closer to the HR references
 280 than common interpolation techniques for three of the four subjects.

Noise std	3	6	9	11	14
Nearest neighbor	3.9×10^{-4}	4.5×10^{-5}	2.8×10^{-6}	1.4×10^{-6}	4.3×10^{-7}
Trilinear	3.2×10^{-4}	2.8×10^{-4}	2.6×10^{-4}	2.8×10^{-4}	3.1×10^{-4}
B-splines	5.4×10^{-1}	6.1×10^{-2}	6.6×10^{-4}	2.0×10^{-5}	2.7×10^{-6}

Table 2: P-values obtained by application of paired t-tests between the RMSE values obtained after the proposed reconstruction and by nearest neighbor interpolation, trilinear interpolation and 3rd order B-splines interpolation, with increasing levels of noise. Standard deviations of noise are expressed as percentage of the GM CBF value.

Method	Subject 1	Subject 2	Subject 3	Subject 4
Nearest neighbor	28.16	26.83	32.19	24.23
Trilinear	26.93	24.80	30.15	22.58
3rd order B-splines	26.34	25.04	29.68	22.49
Proposed method	26.44	24.49	29.12	22.20

Table 3: RMSE values calculated between the HR acquired reference image and the images generated by nearest neighbor interpolation, trilinear interpolation, 3rd order B-splines interpolation and the proposed SR reconstruction method, for each of the 4 healthy subjects (lower RMSE value in bold for each subject).

281 3.3. Comparison with DSC

282 Figure 5 reports, for each of the subjects, the values of the Pearson correlation coefficients obtained between the reference DSC CBF images and
283 the low resolution acquired ASL CBF maps, their interpolations by trilinear
284 and 3rd order B-splines and the images generated with the proposed SR re-
285 construction method. For each subject, the reconstructed image was more
286 correlated to the DSC reference than the others. The significance of the dif-
287 ferences was assessed by applying a Fisher transformation to the correlation
288 coefficients. The p-values obtained after this transformation indicate a sig-
289 nificant difference between the correlation coefficients distributions. Indeed,
290 a paired t-test between the correlation values obtained for the proposed re-
291 constructions and the low resolution acquisitions provided a p-value equal to
292 1.4×10^{-4} , $p = 8 \times 10^{-5}$ by comparison with the trilinear interpolation, and
293 $p = 3.33 \times 10^{-4}$ by comparison with the 3rd order B-splines. Figure 6 dis-
294 plays the DSC CBF images, low resolution ASL CBF maps and CBF maps
295 reconstructed with our method for two of the patients.
296

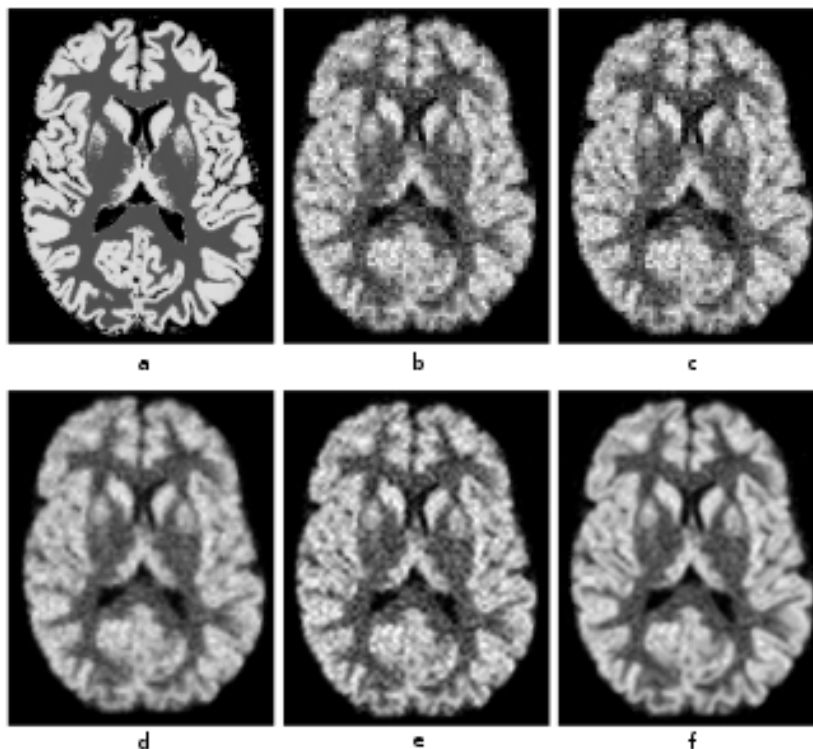


Figure 2: Simulated dataset: comparison of a) a HR reference image and b) the corresponding low resolution downsampled image corrupted by noise with $\text{std}=9\%$ of the GM CBF value, c) nearest neighbor interpolation, d) trilinear interpolation, e) 3rd order B-splines interpolation, and f) proposed SR reconstruction.

297 4. Comparison with Partial Volume Correction methods

298 4.1. Method

299 Typical low resolution ASL acquisitions lead to well known PVE in ASL
 300 images, sometimes unfortunately preventing clinicians to interpret MRI ob-
 301 servations such as reduced CBF values in regions of interest. Indeed, they
 302 could be the consequences of an effective reduced perfusion, a thinner GM
 303 or small subject motion. Because of the fact that the method described in
 304 this paper enables the recovery of high frequency details that are not visible
 305 in low resolution acquisitions, we propose to evaluate the influence of this
 306 recovery on a potential reduction of PVE. This is of particular interest, since
 307 the PVE correction methods that are currently the most commonly applied
 308 to ASL images correct CBF values at the voxel level, thus not providing

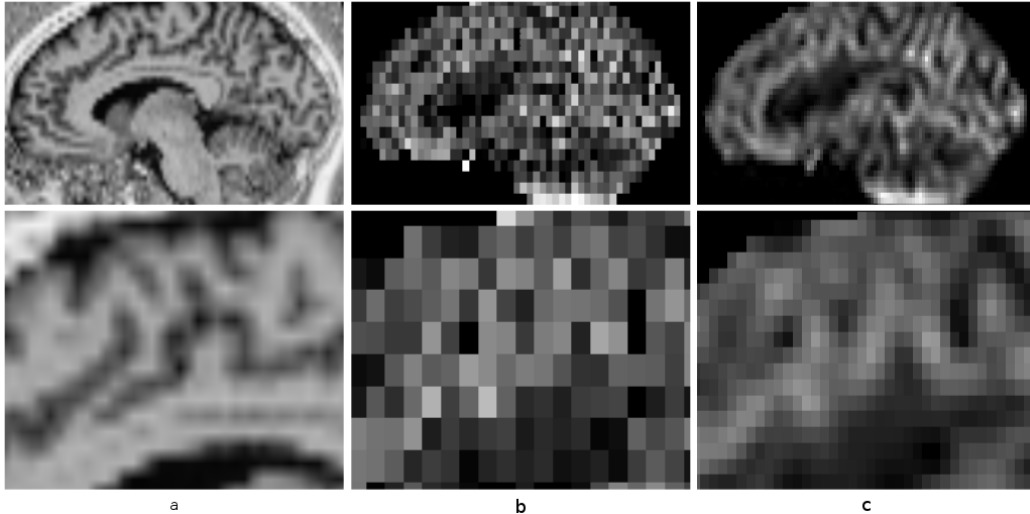


Figure 3: Sagittal slices of a) a structural image, b) the corresponding CBF map from the low resolution ASL acquisition, and c) the proposed SR reconstruction.

309 better detailed images. Moreover, the method that we present in this work
 310 is only dependent on the registration of a HR structural image on an inter-
 311 polated ASL one, while classical PVE correction methods require the use of
 312 tissue PV estimates. These PV estimate maps are provided by segmentation
 313 algorithms, and are therefore subject to potential additional errors.
 314 In order to compare the impact of these algorithms on PVE, a simulation
 315 was conducted from the same 9 structural images as presented in 2.3.1, in
 316 which we aimed at having the most possible information about intensity val-
 317 ues. In order to construct these 9 HR ASL images in which we knew the
 318 exact voxel constitution and associated values, images containing 100% GM
 319 or WM voxels were created, by thresholding the PV estimates generated by
 320 the SPM12 segmentation algorithm. Perfusion maps were generated by af-
 321 fecting ΔM values of 10 for GM and 1.5 for WM, with additional sinusoidal
 322 variations of 20% amplitude to make them more realistic, and evaluate the
 323 capability of the tested algorithms to preserve spatial variations and details
 324 [29]. The same process was used to create M0 images, with values of 1350
 325 and 1000 in GM and WM respectively. These HR perfusion and M0 maps
 326 were downsampled by averaging $2 \times 2 \times 2$ voxel cubes, therefore reducing the
 327 size of the images and adding PVE, while knowing the exact brain tissue mix-
 328 ture of these new low resolution voxels. Different amount of gaussian noise

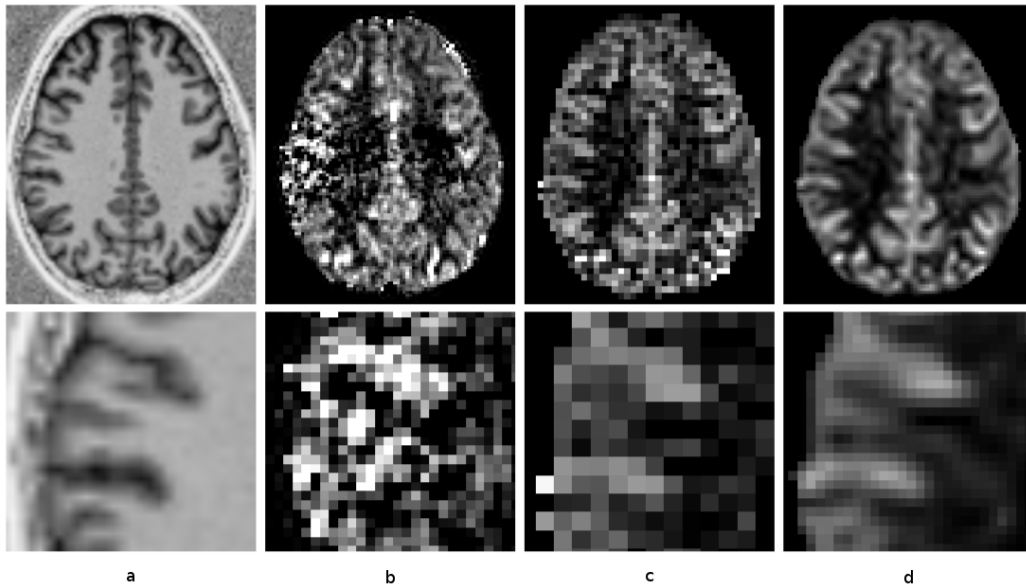


Figure 4: Axial slices of a) a structural image, b) the corresponding CBF maps from the HR and c) low resolution ASL acquisitions, and d) the proposed SR reconstructed image.

329 (SNR=5,10) were added to these images in order to evaluate the influence of
 330 noise on PVE correction. The general kinetic model for pCASL acquisitions
 331 was then applied to obtain the corresponding CBF maps ($\lambda : 0.9$, $\alpha : 0.85$,
 332 $T_{1,blood}$: 1650 ms, LD: 1800 ms, PLD: 1800 ms).

333 The effect of the proposed algorithm on PVE was evaluated by analyzing its
 334 ability to recover the effective GM contribution in the CBF values observed
 335 in each voxel, in comparison with the linear regression method, which is one
 336 of the standard PVE correction technique applied to ASL images [11].

337 Our proposed SR method provides high resolution CBF maps unlike the lin-
 338 ear regression method, which produces two PV maps at the initial resolution.
 339 This is the reason why our SR CBF maps have been downsampled, in order
 340 to be able to compare the two results. The GM contributions in the CBF
 341 maps obtained by applying the general kinetic model to the HR perfusion
 342 and M0 images, without noise, were considered as the references to which
 343 the generated images had to be compared. Figure 7 illustrates the pipeline
 344 that corresponds to the above-mentioned operations.

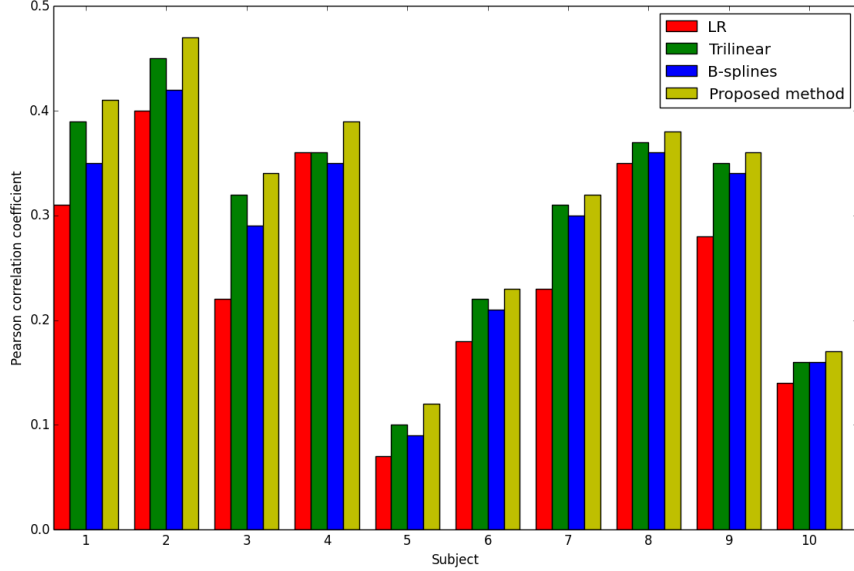


Figure 5: Pearson correlation coefficient between the reference DSC CBF maps and low resolution CBF images, the same images after trilinear interpolation, 3rd order B-splines interpolation and the proposed SR reconstruction method. These coefficients are presented for each of the 10 subjects.

345 4.2. Results

346 Contrary to differences in the produced GM contribution maps reported
 347 in Zhao et al. [29], between an application of the linear regression to the calcu-
 348 lated CBF map and to perfusion and M0 images before the CBF calculation,
 349 our method did not show such significant differences while testing for the
 350 influence of this effect. Figure 8 presents the GM contributions to the CBF
 351 values in a reference image, their recovery by application of the linear regres-
 352 sion method to the low resolution CBF map, by applying the same method
 353 to perfusion and M0 images before CBF calculation, and after increasing
 354 the CBF image dimensions with our method. Figure 9 shows the difference
 355 images obtained after the subtraction of each of the produced images listed
 356 above and the corresponding reference. An important aspect illustrated in
 357 these difference images is the fact, already stated in [11, 12, 13, 29], that the
 358 linear regression method implies a smoothing of the GM contributions. On
 359 the contrary, the sinusoidal variations are retained in the image originating

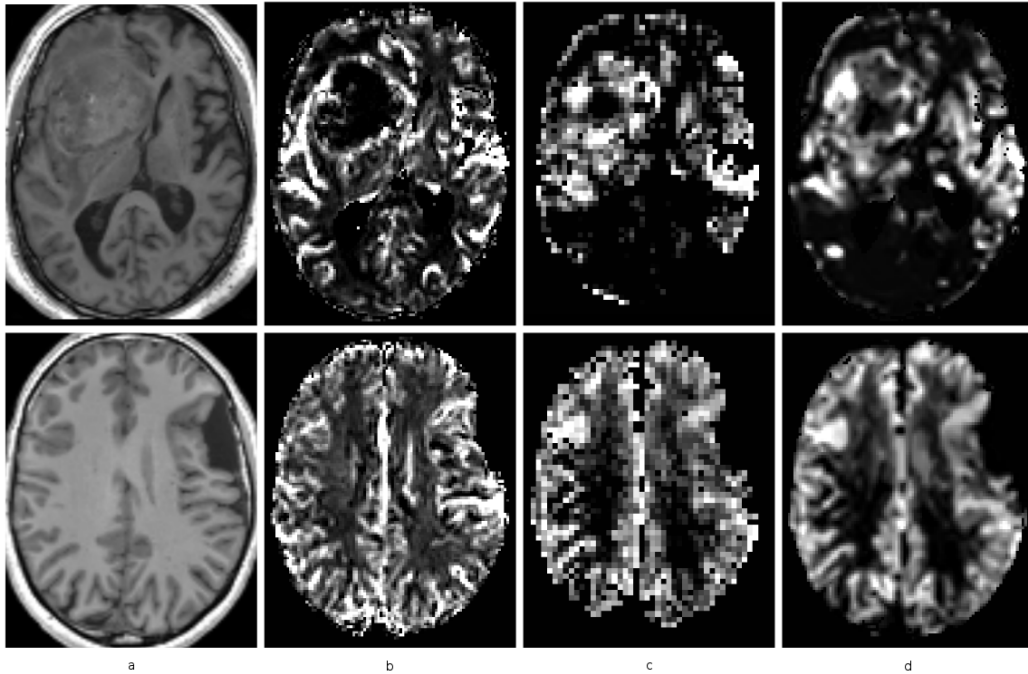


Figure 6: a) structural image, b) DSC CBF image, c) low resolution ASL CBF image and d) SR reconstructed ASL CBF map. The two lines correspond to images of two different subjects.

360 from the proposed algorithm.
 361 Table 4 presents the evolution of the mean RMSE values calculated between
 362 the generated GM contribution images and their references as a function of
 363 noise (SNR=inf, 10, 5). In practice, both applications of the linear regression
 364 method to the CBF maps or to the perfusion and M0 images are commonly
 365 accepted [29]. Since the mean RMSE values obtained by applying our method
 366 to CBF maps are bounded by the mean RMSE provided by these two linear
 367 regressions, we can presume that our method reduces the influence of PVE.
 368 Moreover, the linear regression method is based on the use of information
 369 provided by PV estimates, which makes it dependent upon the chosen seg-
 370 mentation algorithm and sensitive to potential segmentation errors. On the
 371 contrary, our SR reconstruction method is independent of any segmentation
 372 algorithm. In order to investigate the influence of these segmentation cor-
 373 ruptions on the GM contribution maps resulting from the application of the
 374 linear regression, we simulated variations in the segmented PV estimates by

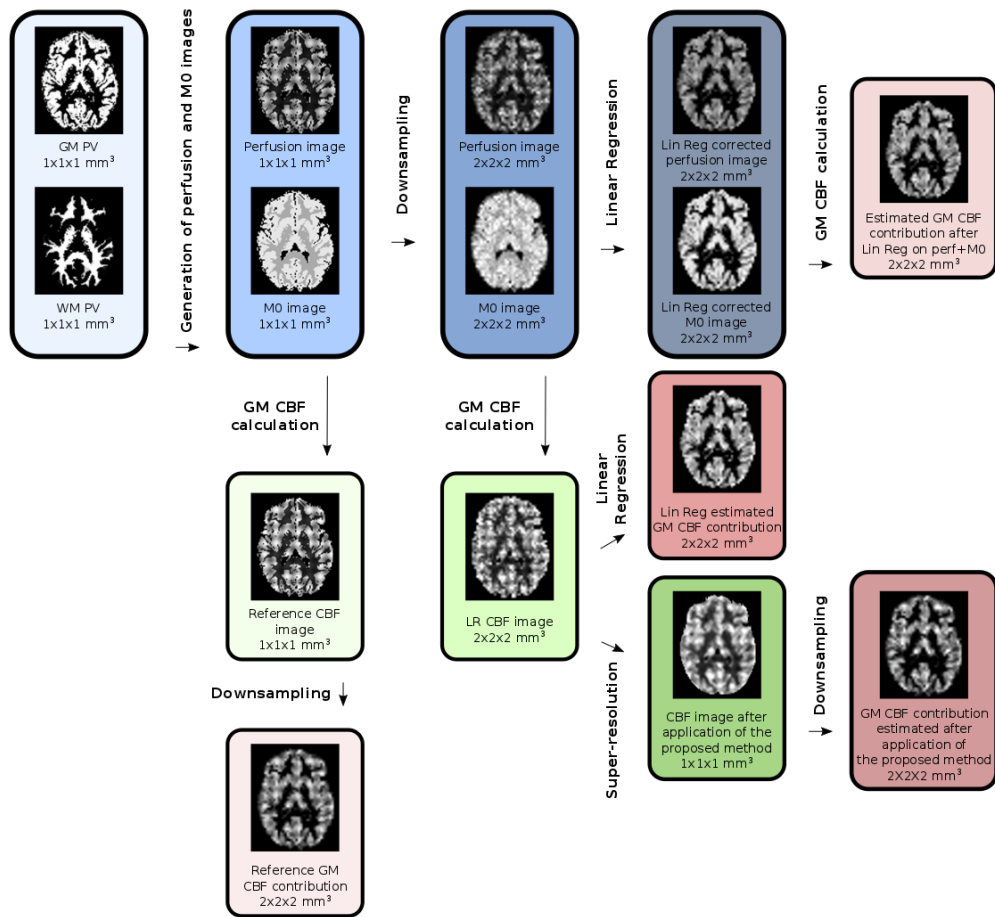


Figure 7: Pipeline describing the operations applied to each of the 9 images of the simulated dataset and the GM contribution assessment maps to be compared.

375 introducing gaussian noise or by applying an opening and closing morphological
 376 operation to these PV maps. Tables 5 and 6 show a significant increase in
 377 the mean RMSE values when the PV estimates are modified. These results
 378 indicate that the property of the SR reconstruction to be independent of the
 379 use of PV estimates could be of great interest to avoid potential errors due
 380 to segmentation corruption.

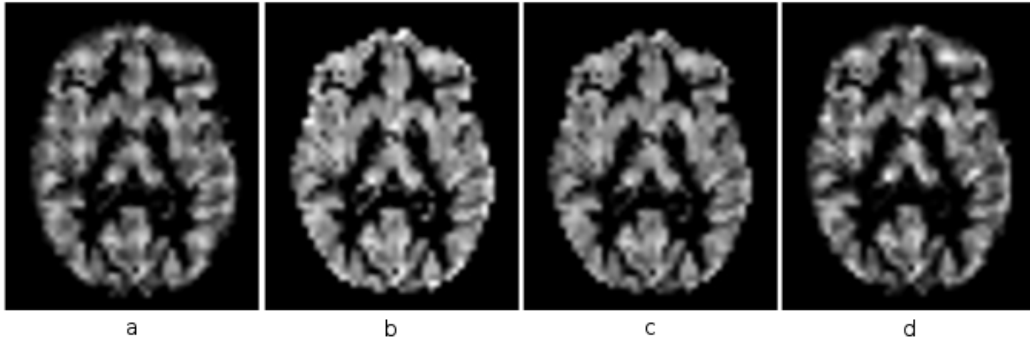


Figure 8: Comparison of gray matter cerebral blood flow contribution maps: a) GM contribution maps from the reference image, b) linear regression applied to the low resolution CBF image, c) linear regression applied to the low resolution perfusion and M0 images, and d) proposed SR method applied to the LR CBF image (SNR=5).

Method	SNR=inf	SNR=10	SNR=5
Lin Reg on CBF	6.41 ± 0.74	6.54 ± 0.75	7.05 ± 0.75
Lin Reg on Perf & M0	4.39 ± 0.17	4.52 ± 0.17	4.90 ± 0.17
SR on CBF	5.66 ± 0.11	5.94 ± 0.13	6.77 ± 0.14

Table 4: Mean RMSE values between the reference GM CBF contribution images and the images obtained after linear regression (Lin Reg) on the low resolution (LR) CBF image, Lin Reg on the perfusion and M0 images, and the proposed SR method applied to the LR CBF images.

Method	SNR=inf	SNR=10	SNR=5
Lin Reg on CBF	7.46 ± 0.60	7.65 ± 0.59	8.09 ± 0.62
Lin Reg on Perf & M0	5.84 ± 0.23	5.97 ± 0.24	6.24 ± 0.22
SR on CBF	5.66 ± 0.11	5.94 ± 0.13	6.77 ± 0.14

Table 5: Mean RMSE values between the reference GM CBF contribution images and the images obtained after linear regression (Lin Reg) on the low resolution(LR) CBF image and on the perfusion and M0 images, with noise added to the PV estimates needed by the Lin Reg method, and the proposed SR method applied to the LR CBF images.

381 5. Discussion

382 In this work, we have presented and investigated different properties of a
 383 SR reconstruction method dedicated to ASL images. This method enables to
 384 increase the level of details, while providing a denoising of the reconstructed
 385 images. It is based on the assumptions of an appearing accordance between

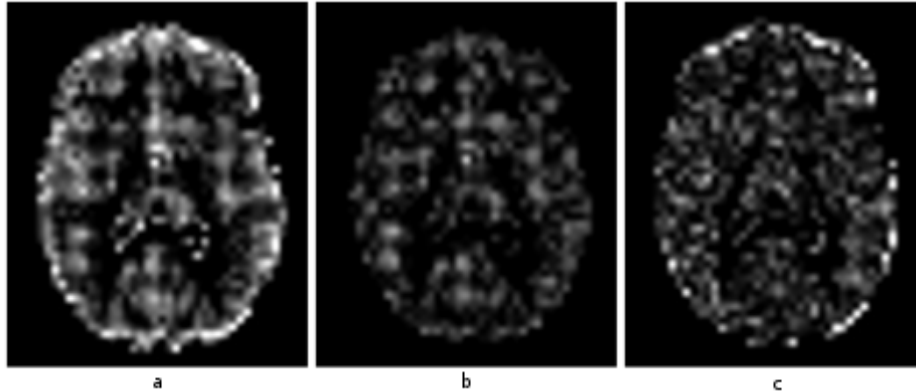


Figure 9: Comparison of gray matter cerebral blood flow contribution maps: a) difference images obtained by subtraction of the reference GM contribution map from the images obtained by applying the linear regression (Lin Reg) to the low resolution (LR) CBF image, b) the linear regression to the LR perfusion and M0 images, and c) the proposed SR method to the LR CBF image (SNR=5).

Method	SNR=inf	SNR=10	SNR=5
Lin Reg on CBF	11.68 ± 0.70	11.78 ± 0.70	12.10 ± 0.75
Lin Reg on Perf & M0	11.19 ± 0.50	11.23 ± 0.49	11.42 ± 0.51
SR on CBF	5.66 ± 0.11	5.94 ± 0.13	6.77 ± 0.14

Table 6: Mean RMSE values between the reference GM CBF contribution images and the images obtained after linear regression (Lin Reg) on the low resolution (LR) CBF image and on the perfusion and M0 images, with an opening+closing operation added to the PV estimates needed by the Lin Reg method, and the proposed SR method applied to the LR CBF images.

386 neighborhoods in the image to be reconstructed and a classically acquired
 387 HR anatomical image, and that distant neighborhoods could serve as a learn-
 388 ing database in the reconstruction process.

389 On a simulated dataset, we have shown that our method provides images
 390 closer to references than common interpolation techniques. The fact that
 391 this result could be obtained with different levels of noise added to the im-
 392 ages to be reconstructed is an indication of the ability of the proposed method
 393 to denoise the reconstructed images.

394 Experiments on low resolution data acquired on healthy subjects confirmed
 395 these findings on 3 over 4 subjects. The main limitation of this study is
 396 nonetheless the relevance of the definition of the HR ASL images as refer-

397 ences, because of their low SNR. In order to maintain the scan time rea-
398asonable and avoid subject motions that would almost certainly happen after
39910 minutes of continuous scanning, 100 control-label repetitions have been
400acquired to generate the high resolution ASL images. This number is cer-
401tainly still not sufficient to obtain an appropriate image quality, which could
402explain the fact that a better RMSE value was obtained by applying a 3rd
403order B-spline interpolation for the first subject. This limitation is precisely
404the reason why we chose to conduct the two other studies, meaning with a
405simulated dataset and the comparison with DSC images.

406The study based on images of patients diagnosed with brain tumors revealed
407a significantly increased correlation between DSC and images reconstructed
408with our method, supporting the capability of the proposed method to re-
409cover details by driving the reconstruction of ASL images with a high res-
410olution structural one. The TI value chosen to acquire these PASL data
411was possibly a little short for subjects 5, 6 and 10, which could explain the
412reduced correlation values obtained for these three subjects.

413We showed that our method associates an increase in the level of details with
414a reduction of the partial volume effect in ASL images. The main advantage
415of this SR reconstruction in comparison with the linear regression partial
416volume correction method is to preserve spatial signal fluctuations, which
417are smoothed by the latter.

418The method proposed in this paper only depends on the accurate registration
419of a HR structural image on the initially interpolated ASL image to be recon-
420structed. Indeed, experiments revealed that the initial interpolation method
421selected in order to increase the dimension of the image to reconstruct does
422not have a significant influence on the generated image, and denoising is
423performed jointly with the details recovery process. This aspect makes our
424method an appropriate tool to increase the quality and the fidelity of ASL
425images, and particularly CBF maps, with respect to effective physiological
426processes. Another promising aspect is its faculty to recover well detailed
427ASL images from standard clinical acquisition protocols, therefore not in-
428creasing the acquisition time and patient discomfort. We believe that such a
429post-processing procedure could help clinicians to establish even more accu-
430rate diagnosis, by reducing interrogations concerning the reasons of reduced
431perfusion values and being able to distinguish GM thickness reduction or an
432effective perfusion reduction for example.

433 6. Acknowledgements

434 This work was supported by Siemens Healthcare France SAS.
435 MRI data acquisition and processing were supported by the Neurinfo MRI
436 research facility from the University of Rennes 1. Neurinfo is granted by the
437 European Union (FEDER), the French State, the Brittany Council, Rennes
438 Metropole, Inria, Inserm and the University Hospital of Rennes.
439 We thank D.J.J. Wang for providing the 2D pCASL sequence used to acquire
440 the images of the healthy subjects [23], E. Bannier for her help in designing
441 the acquisition protocols, B. Carsin for her participation in the acquisition of
442 the DSC data and C. Maumet for the code used to process these DSC data.
443 All the studies conducted in this work were approved by the local Ethics
444 Committee, and all participants provided written informed consent for their
445 data to be used for research work purposes.

446 References

- 447 [1] J. A. Detre, H. Rao, D. J. Wang, Y. F. Chen, Z. Wang, Applications of
448 arterial spin labeled MRI in the brain, *Journal of Magnetic Resonance*
449 *Imaging* 35 (2012) 1026–1037.
- 450 [2] J. A. Detre, J. S. Leigh, D. S. Williams, A. P. Koretsky, Perfusion
451 imaging, *Magnetic Resonance in Medicine* 23 (1992) 37–45.
- 452 [3] H. Raoult, J. Petr, E. Bannier, A. Stamm, J.-Y. Gauvrit, C. Barillot, J.-
453 C. Ferré, Arterial spin labeling for motor activation mapping at 3t with
454 a 32-channel coil: Reproducibility and spatial accuracy in comparison
455 with BOLD fMRI, *NeuroImage* 58 (2011) 157–167.
- 456 [4] R. B. Buxton, L. R. Frank, E. C. Wong, B. Siewert, S. Warach, R. R.
457 Edelman, A general kinetic model for quantitative perfusion imaging
458 with arterial spin labeling, *Magnetic Resonance in Medicine* 40 (1998)
459 383–396.
- 460 [5] L. M. Parkes, P. S. Tofts, Improved accuracy of human cerebral blood
461 perfusion measurements using arterial spin labeling: Accounting for cap-
462 illary water permeability, *Magnetic Resonance in Medicine* 48 (2002)
463 27–41.

- 464 [6] D. C. Alsop, J. A. Detre, X. Golay, M. Gnther, J. Hendrikse,
465 L. Hernandez-Garcia, H. Lu, B. J. MacIntosh, L. M. Parkes, M. Smits,
466 M. J. P. van Osch, D. J. J. Wang, E. C. Wong, G. Zaharchuk, Recom-
467 mended implementation of arterial spin-labeled perfusion mri for clinical
468 applications: A consensus of the isrmr perfusion study group and
469 the european consortium for asl in dementia, *Magnetic Resonance in*
470 *Medicine* 73 (2015) 102–116.
- 471 [7] C. Maumet, P. Maurel, J.-C. Ferr, C. Barillot, Robust estimation of
472 the cerebral blood flow in arterial spin labelling, *Magnetic Resonance*
473 *Imaging* 32 (2014) 497 – 504.
- 474 [8] J. Petr, J.-C. Ferre, J.-Y. Gauvrit, C. Barillot, Improving arterial spin
475 labeling data by temporal filtering, *Proc.SPIE* 7623 (2010) 7623 – 7623
476 – 9.
- 477 [9] A. Buades, B. Coll, J. M. Morel, A review of image denoising algorithms,
478 with a new one, *Multiscale Modeling & Simulation* 4 (2005) 490–530.
- 479 [10] P. Coupe, P. Yger, S. Prima, P. Hellier, C. Kervrann, C. Barillot, An
480 optimized blockwise nonlocal means denoising filter for 3-d magnetic
481 resonance images, *IEEE Transactions on Medical Imaging* 27 (2008)
482 425441.
- 483 [11] I. Asllani, A. Borogovac, T. R. Brown, Regression algorithm correct-
484 ing for partial volume effects in arterial spin labeling mri, *Magnetic*
485 *Resonance in Medicine* 60 (2008) 1362–1371.
- 486 [12] M. A. Chappell, A. R. Groves, B. J. MacIntosh, M. J. Donahue, P. Jez-
487 zard, M. W. Woolrich, Partial volume correction of multiple inversion
488 time arterial spin labeling mri data, *Magnetic Resonance in Medicine*
489 65 (2011) 1173–1183.
- 490 [13] J. Petr, J.-C. Ferre, J.-Y. Gauvrit, C. Barillot, Denoising arterial spin
491 labeling mri using tissue partial volume, *Proc.SPIE* 7623 (2010) 7623 –
492 7623 – 9.
- 493 [14] B. Scherrer, A. Gholipour, S. K. Warfield, Super-resolution reconstruc-
494 tion to increase the spatial resolution of diffusion weighted images from
495 orthogonal anisotropic acquisitions, *Medical Image Analysis* 16 (2012)
496 1465–1476.

- 497 [15] F. Rousseau, A non-local approach for image super-resolution using
498 intermodality priors, *Medical Image Analysis* 14 (2010) 594–605.
- 499 [16] J. V. Manjón, P. Coupé, A. Buades, D. L. Collins, M. Robles, MRI su-
500 perresolution using self-similarity and image priors, *International Jour-
501 nal of Biomedical Imaging* 2010 (2010) 1–11.
- 502 [17] P. Coupé, J. V. Manjón, M. Chamberland, M. Descoteaux, B. Hiba, Col-
503 laborative patch-based super-resolution for diffusion-weighted images,
504 *NeuroImage* 83 (2013) 245–261.
- 505 [18] M. Protter, M. Elad, H. Takeda, P. Milanfar, Generalizing the nonlocal-
506 means to super-resolution reconstruction, *IEEE Transactions on Image
507 Processing* 18 (2009) 36–51.
- 508 [19] C. Meurée, P. Maurel, C. Barillot, Patch-based super-resolution for
509 arterial spin labeling MRI , *ISMRM 25th Annual Meeting & Exhibition
510* (2017).
- 511 [20] J. P. Marques, T. Kober, G. Krueger, W. van der Zwaag, P.-F. V.
512 de Moortele, R. Gruetter, MP2rage, a self bias-field corrected sequence
513 for improved segmentation and t1-mapping at high field, *NeuroImage*
514 49 (2010) 1271–1281.
- 515 [21] L. M. Parkes, W. Rashid, D. T. Chard, P. S. Tofts, Normal cerebral
516 perfusion measurements using arterial spin labeling: Reproducibility,
517 stability, and age and gender effects, *Magnetic Resonance in Medicine*
518 51 (2004) 736–743.
- 519 [22] *Statistical Parametric Mapping: The Analysis of Functional Brain Im-
520 ages*, Academic Press, 2006.
- 521 [23] W.-C. Wu, M. Fernández-Seara, J. A. Detre, F. W. Wehrli, J. Wang,
522 A theoretical and experimental investigation of the tagging efficiency
523 of pseudocontinuous arterial spin labeling, *Magnetic Resonance in
524 Medicine* 58 (2007) 1020–1027.
- 525 [24] L. Østergaard, R. M. Weisskoff, D. A. Chesler, C. Gyldensted, B. R.
526 Rosen, High resolution measurement of cerebral blood flow using in-
527 travascular tracer bolus passages. part i: Mathematical approach and
528 statistical analysis, *Magnetic Resonance in Medicine* 36 (1996) 715–725.

- 529 [25] C. Warmuth, M. Günther, C. Zimmer, Quantification of blood flow
530 in brain tumors: Comparison of arterial spin labeling and dynamic
531 susceptibility-weighted contrast-enhanced MR imaging, *Radiology* 228
532 (2003) 523–532.
- 533 [26] K. Gorgolewski, C. D. Burns, C. Madison, D. Clark, Y. O. Halchenko,
534 M. L. Waskom, S. S. Ghosh, Nipype: A flexible, lightweight and exten-
535 sible neuroimaging data processing framework in python, *Frontiers in*
536 *Neuroinformatics* 5 (2011).
- 537 [27] F. Q. Ye, K. F. Berman, T. Ellmore, G. Esposito, J. D. van Horn,
538 Y. Yang, J. Duyn, A. M. Smith, J. A. Frank, D. R. Weinberger, A. C.
539 McLaughlin, H215o pet validation of steady-state arterial spin tagging
540 cerebral blood flow measurements in humans, *Magnetic Resonance in*
541 *Medicine* 44 (2000) 450–456.
- 542 [28] C. Maumet, P. Maurel, J.-C. Ferré, C. Barillot, An a contrario approach
543 for the detection of patient-specific brain perfusion abnormalities with
544 arterial spin labelling, *NeuroImage* 134 (2016) 424–433.
- 545 [29] M. Y. Zhao, M. Mezue, A. R. Segerdahl, T. W. Okell, I. Tracey, Y. Xiao,
546 M. A. Chappell, A systematic study of the sensitivity of partial vol-
547 ume correction methods for the quantification of perfusion from pseudo-
548 continuous arterial spin labeling MRI, *NeuroImage* 162 (2017) 384–397.